This document is complies with the paper:

author's email: simone.siriano@uniroma1.it

Electromagnetic coupling phenomena in co-axial rectangular channels

Simone Siriano[a*], Alessandro Tassone[a], Gianfranco Caruso[a], Alessandro Del Nevo[b]

[a]*Department of Astronautical, Electrical and Energy Engineering, Sapienza University of Rome, Rome, Italy*
[b]*ENEA FSN-ING-PAN, ENEA CR Brasimone, Camugnano, Italy*

In the Water-Cooled Lithium Lead (WCLL) blanket, the eutectic alloy lithium-lead (PbLi) is used as tritium breeder and carrier, neutron multiplier and heat transfer medium. The liquid metal is distributed to and collected from the breeding zone through a compact poloidal manifold composed of two co-axial rectangular channels. The external channel, tasked with distribution, and the internal one, assigned to the collection, are co-flowing and share an electrically conductive wall ($c_w = 0.1$). The liquid metal, interacting with the reactor magnetic field, leads to the arising of MagnetoHydroDynamic (MHD) effects that are expected to significantly modify the flow feature and electrically couple the external and internal channels. In this work, the general-purpose CFD code Ansys CFX 18.2 is used to study the coupling phenomena in a wide range of magnetic fields (up to $Ha = 2000$) for a prototypical square co-axial channel. Characteristic flow features and their evolution with increasing magnetic field and varying mass flow rate between the channels are discussed and compared with the uncoupled case, which is in turn composed by a rectangular electro-conductive annulus (external) and a square electro-conductive duct (internal). A correlation is found linking the pressure loss in the studied configuration and an equivalent square channel through a corrective factor ε, which exhibits an asymptotic behavior for $Ha > 1000$.

Keywords: Electro-coupling, DEMO, Magnetohydrodynamic (MHD), Manifold, PbLi, WCLL

1. Introduction

The Breeding Blanket (BB) is one of the key components of a nuclear fusion reactor, since it has the tasks of producing and extracting the tritium and thermal power generated therein. In the Water-Cooled Lead Lithium (WCLL) concept, PbLi is employed as tritium breeder/carrier and neutron multiplier, whereas pressurized water cools the system. The current design (2018), based on DEMO 2017 specifications and derived from R&D activities conducted in the framework of the EUROfusion Programme, relies on the Single Module Segment approach, with a breeding element repeated along the poloidal direction [1]. The liquid metal is distributed to the elementary cells composing the Breeding Zone (BZ) through a compact poloidal manifold constituted by two long co-axial rectangular channels that fulfill both the distribution and collection task (Fig. 1A).

A liquid metal that flows through a magnetic field, as the one in the fusion reactor, leads to the appearance of MagnetoHydroDynamic (MHD) effects, which significantly influence the flow features. Indeed, the magnetic field induces electric currents in the metal that, in turn, interact with the magnetic field and generate a Lorentz force, which changes the force balance in the fluid. Moreover, the Lorentz force is not uniformly distributed on the channel cross-section but, rather, it is dependent on the overall magnitude and paths of the current inside the fluid, which, in turn, depends on the electric conductivity of the walls. When two or more channels are electrically connected by a common conductive wall, currents generated in one fluid body can be exchanged with adjacent ones and, therefore, influence their flow features. These "leakage currents" make such channels electromagnetically coupled that is fluid motion in one channel is no longer univocally determined by the current field internally generated (Madarame effect).
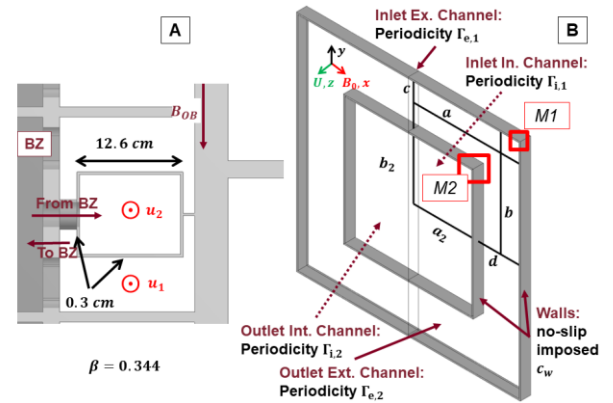

Fig. 1. PbLi manifold co-axial channel detail without water tubes (A), computational domain with BCs and velocity profile sampling locations (B).

The first study on MHD coupled flow is the seminal work by Madarame et al. [2] (1985) that demonstrated how pressure loss in a simple square orifice can be greatly magnified by the interaction with nearby channels. The first studies considering this effect on the manifold are those of McCarthy and Abdou [3] (1991) and Molokov [4] (1993), that investigated the global influence of leakage currents in a manifold composed by square channels and found that flow distribution is also affected. Recently, Bluck and Wolfendale [5] have analytically investigated a coupled array of ducts, in both co- and counter-flow configurations, stacked parallel to the applied magnetic field, where these ducts have insulated side walls and conducting Hartmann walls. Mistrangelo and Buhler [6] numerically studied a similar configuration with an arbitrary orientation of the magnetic field and direction of driving pressure gradients. Swain et al.[7] (2018) have been performed numerical simulation and experiments at high magnetic fields for PbLi flow in coupled co- and counter-flow configuration, L- and U-

---

type bend. Studies dealing with a co-axial coupled channel are scarcer compared with duct arrays. One of the few examples of note is Chen et al. [8] that investigates the MHD phenomena in an assembly composed by three co-axial counter-flowing rectangular channels electrically decoupled or coupled from each other through multi-layer flow channel inserts of arbitrary conductivity.

In this paper, the MHD electro-coupled forced convection flow in co-axial and co-flowing annular configuration is studied. Numerical simulations are performed for a wide range of magnetic field intensity ($Ha = 100 \div 2000$) and with a finite electrical conductivity for both the internal and external walls, as foreseen in the WCLL current design, using the general CFD code ANSYS CFX 18.2. A similar model has been used in [9] to study the basic phenomena in an uncoupled annular channel and it has been updated to account for the inner channel effect in this work that can be considered as an extension of [9].

A correct estimate of the MHD pressure drop is critical to design the WCLL PbLi loop and, therefore, an accurate prediction of the losses in the manifold is required since these account for the bulk of the blanket contribution [10]. The pressure gradient calculated by the CFD code for both the external annular channel (∇p_e^n) and the internal one (∇p_i^n), is compared with the analytical value calculated for the fully developed flow neglecting coupling phenomena. For the annular channel, the theoretical value (∇p_e) is computed from an equivalent square duct, whereas it is directly calculated for the internal one (∇p_i). Engineering correction factors ($\varepsilon_{e,i} = \nabla p_{e,i}^n / \nabla p_{e,i}$) are defined to express the relationship between the flow in co-axial, coupled, channels and the flow in square, uncoupled, conduits. Then, it is demonstrated that these correction factors are invariant at $Ha > 10^3$. This allows to extrapolate our results at higher field intensity, thus making possible to calculate the co-axial manifold pressure loss from analytical correlation.

2. Numerical model

The geometry of the WCLL 2018 design manifold external channel is quite complex featuring several conductive obstacles and an asymmetric layout (Fig. 1A). To characterize the influence of the electro-coupling phenomena the manifold external channel is simplified to its more basic analogue: a square annular channel with the same internal width, blockage ratio β and internal wall thickness (Fig. 1A) with respect to the original channel and without obstacles to streamline the configuration. The resulting equivalent model is shown in Fig. 1B and its geometrical parameters are collected in Table 1.

Since PbLi, which physical properties are reported in Table 2, is progressively distributed moving toward the top of the blanket, it is possible to assume that the external channel flow rate (Γ_e) is decreasing linearly without introducing any significant error compared with a more realistic step function. At the same time, the breeder passes from the BZ to the inner channel where, similarly, the mass flow rate (Γ_i) increases with the same law. Therefore, the two manifold sub-channel flow rates are

linked and, for an arbitrary position along the poloidal direction, their sum must satisfy the relation $\Gamma_{tot} = \Gamma_e + \Gamma_i$, where Γ_{tot} is the imposed mass flow rate in the blanket. In the following, simulation scenarios at different poloidal heights are going to be labelled with the external channel flow rate expressed as a percentage of the total one. For instance, $\Gamma_e = 0.5\Gamma_{tot}$ refers to the situation in which half of the flow rate is carried by the external channel and, similarly, the other half is found in the internal one. Flow in these two sub-channels is co-flowing along the z-direction, isothermal, steady and fully developed and moves through a uniform and steady magnetic field $\boldsymbol{B}$ applied on the x-direction.

Table 1. Geometrical parameters of the annular channel.

Parameter	Symbol	Value (unit)
Aspect ratio	$\alpha = a/b = a_2/b_2$	1
Blockage ratio	$\beta = a_2^2/a^2$	0.344
External side	$2a$	21.48 (cm)
Internal side	$2a_2$	12.30 (cm)
Internal gap	$c = d$	4.44 (cm)
Walls thickness	t_w	0.15 (cm)

Table 2. Material properties of PbLi at 600 K [11].

Property	Symbol	Value (unit)
Density	ρ	9806 (kg/m^3)
Viscosity	μ	$1.96 \cdot 10^{-3}$ ($Pa\ s$)
Electrical conductivity	σ	$8.75 \cdot 10^5$ (S/m)

Table 3. Scale velocities and Reynold numbers for the external channel (u_e) and internal channel (u_i) for all the cases.

Case	Channel	$u_{e,i}$ ($10^{-6} m/s$)	Re
$\Gamma_e = \Gamma_{tot}$	External	1.86	1.00
	Internal	1.86*	1.00
$\Gamma_e = 0.75\Gamma_{tot}$	External	1.39	0.75
	Internal	0.928	0.50
$\Gamma_e = 0.5\Gamma_{tot}$	External	0.928	0.50
	Internal	1.86	1.00
$\Gamma_e = 0.25\Gamma_{tot}$	External	0.464	0.25
	Internal	2.78	1.50
$\Gamma_e = 0\Gamma_{tot}$	External	0.928*	0.50
	Internal	3.71	2.00
*These values are calculated assuming $\Gamma_e = 0.5\Gamma_{tot}$			

2.1 Governing equations and dimensionless groups

The MHD governing equations are implemented in the code introducing the Lorentz force as a body force source term in the momentum equation and additional equations for the electric potential φ and current density $\boldsymbol{j}$ (Ohm's Law) [12]. Under the assumptions considered in this work, the inductionless approximation is applicable and, therefore, the dimensionless governing equations used by the code are expressed as [12] [13]

$$\frac{1}{N}\left[\frac{\partial \boldsymbol{u}}{\partial t} + (\boldsymbol{u} \cdot \nabla)\boldsymbol{u}\right] = -\nabla p + \frac{1}{Ha^2}\nabla^2 \boldsymbol{u} + \boldsymbol{j} \times \boldsymbol{B} \quad (1)$$

$$j = -\nabla\varphi + u \times B \qquad (2)$$

$$\nabla^2\varphi = \nabla \cdot (u \times B) \qquad (3)$$

where p is the pressure, u the velocity field and $L_c = a$ the characteristic length, that is the half-width of the model aligned with the magnetic field, excluding walls (Table 1).

$N = \sigma L_c B^2/\rho u$ is the interaction parameter (or Stuart number) and gives the ratio of the electromagnetic forces to the inertia forces, $Ha = L_c B\sqrt{\sigma/\mu}$ is the Hartmann number that represents the ratio of the electromagnetic forces to the viscous forces and characterizes the boundary layer thickness. Characteristic velocity $u_{e,i}$ is the mean velocity which, depending on the value of the imposed mass flow rate, assumes two different values for the external and internal channel, respectively u_e and u_i, as shown in Table 3. Regarding the $\Gamma_e = \Gamma_{tot}$ case, where the fluid in the inner channel would be stagnant in the absence of electromagnetic coupling, it has been chosen as velocity scale the average velocity of the inner channel of the $\Gamma_e = 0.5\Gamma_{tot}$ case. A similar choice was also made for the $\Gamma_e = 0$ case regarding the scaling velocity of the external channel.

In WCLL, these dimensionless numbers assume the values: $Re \cong 5000$, $Ha \cong 9000$ and $N \gg 1$. Therefore, manifold MHD flow is expected to be inertialess and this condition is maintained in our model, even for low Ha simulations, by proper scaling the overall imposed mass flow rate such as it is shown in Table 3 that collects Reynolds numbers for all the cases, all close to unity. The characteristic length used for the Re calculation is still a (Table 1).

At the walls perpendicular to B (Hartmann walls) the boundary layer (Hartmann layer, HL) width is $\delta_H = L_c/Ha$, whereas for walls parallel to B (side walls) the boundary layer (side layer, SL) width is $\delta_S = L_c/\sqrt{Ha}$. The influence of the electrical conductivity of the walls is represented by the conductance ratio $c_w = (\sigma_w t_w)/(\sigma L_c)$, where σ_w and t_w are, respectively, the wall conductivity and thickness. This parameter is assumed uniform in the model, whereas the opposite case is more commonly encountered in practice, as shown in Fig. 1A.

2.2 Mesh and boundary conditions

The mesh adopted is non-uniform, structured and composed by hexahedral elements, which are stretched to provide a finer resolution near the walls to resolve the boundary layers (**Errore. L'origine riferimento non è stata trovata.**). A mesh sensitivity study was performed for the perfectly insulated annular channel at $Ha = 50$ in Ref. [9]. Since no analytical solution is available for code validation, the pressure gradient is chosen as control parameter. Table 4 shows the results. It was found that between 5 and 7 elements in the HL and at least 20 elements in the SL are necessary to achieve good results. The latter HL resolution has been adopted for this study.

Fig. 1B shows the boundary conditions (BCs). No-slip ($u = 0$) is used for all the walls whereas translation

periodicity with a fixed flow rate (for instance, $\Gamma_{e,1} = \Gamma_{e,2}$) is established between the inlet and outlet surface in order to represent a fully-developed flow, thus simulating an infinite length channel.
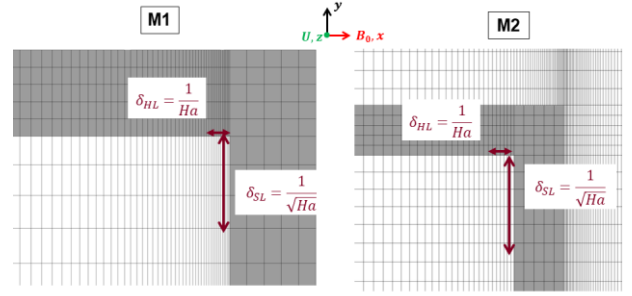

Fig. 2 Mesh detail at M1 and M2 location in Fig.1B.

Table 4. Results of mesh sensitivity study, errors related to the 8 HL subdivisions case.

HL sub.	Pressure gradient Error [%]	Mesh elements
0	No convergence	9954
1	No convergence	18480
2	1.85	26520
3	0.91	33288
4	0.54	40320
5	0.16	49128
6	0.02	58200
7	≈ 0	67392
8	0.00 (reference)	72576

A uniform and finite wall conductivity is assumed ($c_w = 0.1$) for both internal and external walls by imposing a fictitious electrical conductivity of $6.26 \cdot 10^6\ S/m$. These assumptions are not realistic since the external channel walls are characterized by non-uniform thickness and the plate separating the two co-axial channels would be characterized by $c_w \cong 0.01$. However, it was judged to be suitable at this stage to focus on a slightly simplified model to characterize the basic phenomena and consider a more detailed representation of the WCLL manifold in a future study.

Eq. 3 is solved through the coupling of the solid (representing the duct walls) and fluid computational domain where, at the interface, is applied the "conservative interface flux" condition, which enforces current normal ($j_{n1} = j_{n2}$) and electric potential conservation ($\varphi = \varphi_w$) [14].

3. Parametric analysis

3.1 Variable flow rate, fixed Ha

Errore. L'origine riferimento non è stata trovata. shows the velocity contour for $Ha = 2000$ and for different combinations of total mass flow rate (velocity scales for each case are listed in Table 3), whereas **Errore. L'origine riferimento non è stata trovata.** and **Errore. L'origine riferimento non è stata trovata.** show the velocity distribution along four sampling locations, as shown in Fig. 1B and Fig. 3, respectively for the external and internal channel. Since the flow is symmetrical with

respect to $x = 0$, the results are shown on half of the channel. The velocity is scaled with the respective physical mean velocity $u_{e,i}$, collected in Table 3, and the lengths are the linear coordinate of the sampling lines which have the same direction of the respective axes (Fig. 1B and 3). The external channel velocity profiles are compared with the uncoupled case (NC) analyzed in Ref. [9], while the internal channel velocity profiles are compared with the analytical solution provided in Ref. [15] for the uncoupled flow in a square channel of arbitrary conductivity.

The case where all the flow rate is inside the external channel ($\Gamma_e = \Gamma_{tot}$) is practically coincident to the uncoupled case (NC) analyzed in Ref. [9], as can be seen from **Errore. L'origine riferimento non è stata trovata.**. Two high-velocity jets develop at the channel walls aligned with B (Fig. 3) and, between these jets, the hydraulic flow develops into two uniform cores, a faster slug flow in the sub-channels parallel to B (C1) and a slower slug flow in the channel region perpendicular to B (C2). This similitude can be explained from the topology of electric current field in the external channel that is almost equal for these two cases (cfr. Fig. 7 in Ref. [9] and **Errore. L'origine riferimento non è stata trovata.**).

Regarding the current topology in the external channel, we can identify current loops entirely restricted within the fast core C1 (black line), an external current loop (orange line) which occupies almost the entire external channel and an internal loop confined in the slow core C2 (red line). These last two loops flow through the internal side wall but in the opposite direction and converge toward two critical points, marked with diamonds, placed into the top and bottom internal side wall, from which currents leak into the inner channel. Indeed, the fluid therein can no longer be described as stagnant since, even if the net mass flow rate is still equal to zero, leakage currents (white lines Fig. 6) play the role of a momentum source causing the formation of characteristic features shown in Fig. 3: downward jets at walls parallel to the magnetic field (marked with a black line) and upward slug flow in the duct core. The inner channel current field, that is generated by this movement, does not affect the velocity distribution in the external annular channel, which is practically coincident to what was described for the uncoupled channel in [9] as it can be seen in Fig. 4.

This behavior is also mirrored in the $\Gamma_e = 0$ case, where the driving pressure gradient is confined into the internal channel. **Errore. L'origine riferimento non è stata trovata.** shows that leakage currents (white lines) are now dominating the external channel, whereas the potential and the internal channel currents assume the classic electroconductive duct structure, with straight current paths normal to B in the core that close preferentially through the conductive walls (red line). This topology leads to classic velocity distribution in the internal channel, as can be seen from the comparison with the uncoupled analytical solution (Ref. [15]), where two high-velocity jets develop at the wall aligned with B with a damped core between them (**Errore. L'origine**

riferimento non è stata trovata. and **Errore. L'origine riferimento non è stata trovata.**b). The liquid metal in the external channel, initially stagnant, it is pulled by the coupling phenomena, leading to two high reverse jets at the internal side walls (Fig. 3), a reverse flow zone which affects about the half part of the external channel aligned with B (cross in **Errore. L'origine riferimento non è stata trovata.**) and co-flowing flow in the rest of the channel.
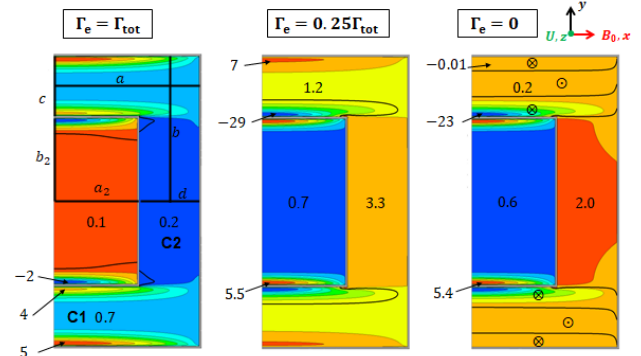

Fig. 3 Velocity contour for $Ha = 2000$ for half channel. Counter flow area inside the black line and dimensionless value for the velocity with different scales for the extern channel. (u/u_e) and for the internal channel (u/u_i) as in Table 3. Velocity profile sampling locations in the picture on the left.
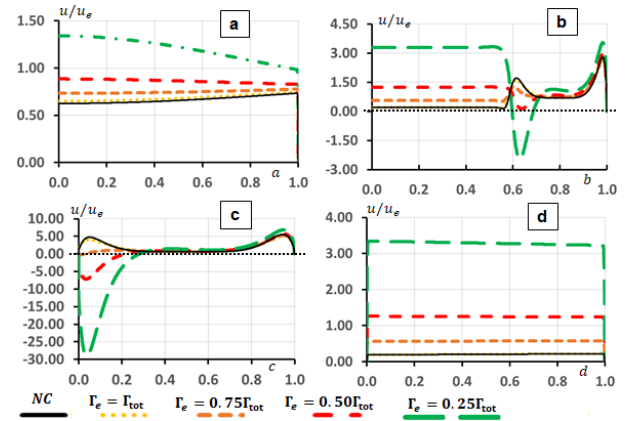

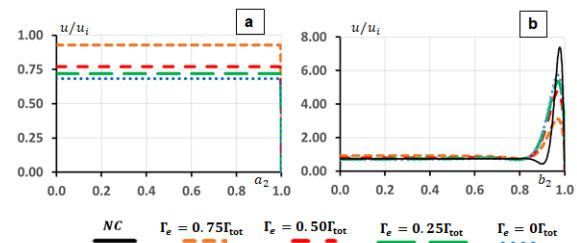Fig. 4 External channel velocity distribution at a, b, c and d for $Ha = 2000$ for half channel.

Fig. 5 Internal channel velocity distribution at a_2 (a) and b_2 (b) for $Ha = 2000$ for half channel.

These two limiting situations ($\Gamma_e = \Gamma_{tot}$ and $\Gamma_e = 0$) are gradually reached due to the transfer of flow from the external to the internal channel. The internal channel is relatively less sensitive to the influence of leakage currents compared with the external one. Already for a

weak internal flow rate ($\Gamma_e = 0.75\Gamma_{tot}$), the internal velocity distribution loses the characteristic coupling features described earlier (Fig. 3) and assumes the classic electroconductive duct structure (Fig. 5), with a core that practically coincides with the uncoupled case and a damped velocity jet on the side walls. Instead, the flow features in the external channel change more clearly when reducing the imposed flow rate.
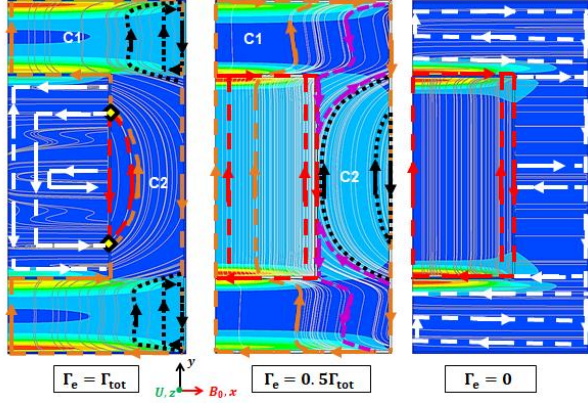

Fig. 6 Contour of the magnitude of electric potential gradient and current streamlines for $Ha = 2000$ with critical point (diamonds) for half channel.

For $\Gamma_e = 0.75\Gamma_{tot}$, the velocity in both the cores starts to increase, the slower one (C2) more markedly, leading to a similar value (Fig. 4b). The jet near the side wall common with the internal channel disappears, practically aligning with the core and the onset of a counter flow is observed (Fig. 4c). The jet on the external side wall, on the other hand, remains practically unchanged.

For $\Gamma_e = 0.50\Gamma_{tot}$, the C2 core becomes larger than the C1 core (Fig. 4b and 7), the jet at the external side wall increases slightly whereas the reverse jet appears at the side wall shared with the internal channel with its associated reverse flow (Fig. 4c and **Errore. L'origine riferimento non è stata trovata.**). The flow features of the internal channel, as the mass flow rate increases, continue to approach those of the uncoupled case (Fig. 5b). These trends increase in agreement with the decrement in the flow rate of the external channel, as shown for $\Gamma_e = 0.25\Gamma_{tot}$ case reported in **Errore. L'origine riferimento non è stata trovata.**, where the reverse velocity jet in the external channel is quite relevant (Fig. 4c) and the velocity in C2 becomes much higher than that in C1 (Fig. 4b).

These phenomena can be explained by analyzing the changing in the external current (**Errore. L'origine riferimento non è stata trovata.**) and electric potential gradient field topology, reported in **Errore. L'origine riferimento non è stata trovata.** as a contour of the magnitude and in **Errore. L'origine riferimento non è stata trovata.** as y-component distribution along the total extent of the co-axial channel ($b_2 + c$ in Fig. 1). Indeed, while these topologies of the internal channel are immediately analogous to the uncoupled electroconductive case, that of the external channel change considerably. The y-component of the electric

potential gradient changes its sign at the proximity of the internal side wall from a positive value for $\Gamma_e = \Gamma_{tot}$ to a negative one as the flow rate increases within the internal channel. These modifications are less conspicuous in the core and in the external side layer In the internal channel, the inversion near the side layer is present only in the case of initially stagnant flow ($\Gamma_e = \Gamma_{tot}$). These phenomena directly impact the Lorentz force component depending on the electric potential gradient (Eq. 1, 2) and causes the appearance of the counter flow jet at the external-side of the partition wall whereas, the other regions of the annular channel undergo, like the potential, a less marked change.
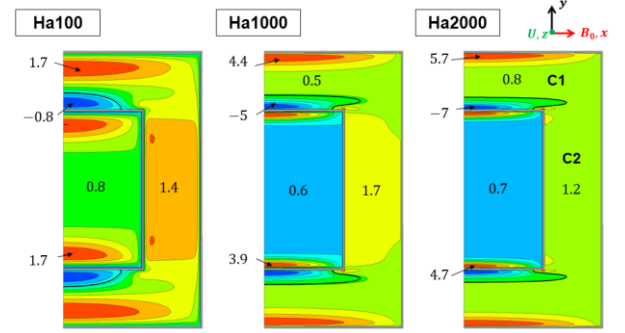

Fig. 7 Velocity contour for $\Gamma_e = \Gamma_i = 0.5\Gamma_{tot}$ for half channel. Counter flow area inside the black line. Dimensionless value for the velocity with different scales for the extern channel (u/u_e) and for the internal channel (u/u_i).
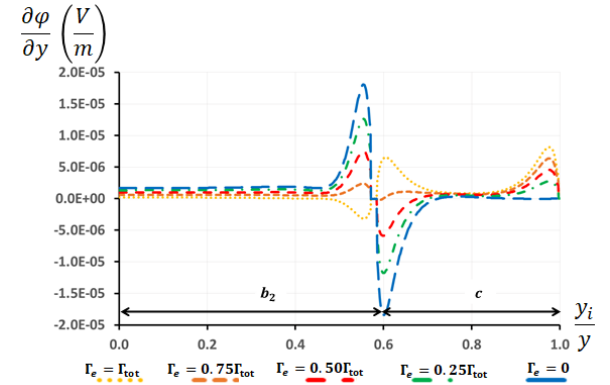

Fig. 8 Y-component of electric potential gradient distribution at the total co-axial channel length $b_2 + c$.

Similar behavior is observed in the internal channel as well, but is significant only when its associated flow rate is very low, and the flow structure differs considerably from the uncoupled case.

The rearrangement of the velocity distribution between the two cores, going from $\Gamma_e = \Gamma_{tot}$ to lower values, can probably be explained with the modification of the current field through the Lorentz force term $\boldsymbol{j} \times \boldsymbol{B}$ of the momentum equation (1). The loops previous shared from both C1 and C2 are now restricted to C2 (black line in Fig. 6 $\Gamma_e = 0.5\Gamma_{tot}$) causing the reversal of the currents that flow through the internal side wall. A new topology of current paths is generated in the external channel (magenta line in Fig. 6), that flows in both C1 and C2 and close through the external and internal Hartmann walls, but do not enter in the internal channel. At the same time,

the inner channel currents do not penetrate the external channel (red line), whereas some current line exit from the bottom external side wall and connect to the top one passing through the inner channel (orange line).

3.2 Fixed flow rate, variable Ha

Errore. L'origine riferimento non è stata trovata. shows the velocity contour with increasing Hartmann number and with a fixed mass flow rate $\Gamma_e = \Gamma_i = 0.5\Gamma_{tot}$. The velocity is scaled with the respective mean velocity $u_{e,i}$.

The internal channel shows features that are analogous to the uncoupled classic electroconductive flow, as already mentioned in Section 3.1. Increasing Ha, two high-velocity jets develop at the internal channel walls aligned with the magnetic field, with a velocity peak about 4.7 times higher than the internal average velocity for $Ha = 2000$. Between these jets the velocity is almost constant.

Regarding the external channel, the reverse jet peak velocity increase with Ha from $-0.8u_e$ at $Ha = 100$ to $-7u_e$ at $Ha = 2000$ (**Errore. L'origine riferimento non è stata trovata.**). Correspondingly, the percentual value of their mass flow rate, with respect to the overall external channel flow rate, goes from 2% at $Ha = 100$ to 19% at $Ha = 2000$. Increasing Ha leads to progressive formation of a jet at the external side wall, as in the uncoupled case [9], but with a lower intensity due to the fact that, even if there is a reverse flow zone much larger than in the uncoupled case, the velocity in the rest of the duct (C1 and C2) is overall higher.

4. Pressure drop analysis: correction factor ε

In order to estimate the MHD pressure drop in WCLL manifold, a relation is tentatively proposed between the pressure gradient calculated by the CFD code ($\nabla p_{e,i}^n$), for both the external annular and internal channel, and the theoretical value ($\nabla p_{e,i}$) [16]. This value is computed for the fully developed flow in an equivalent square duct for the external annular channel and for the same channel without considering the coupling phenomena for the internal channel. This relation is defined through the correction factor $\varepsilon_{e,i} = \nabla p_{e,i}^n / \nabla p_{e,i}$ which, in general, will assume a different value depending on the model geometrical parameters (e.g. aspect and blockage ratio). If this factor becomes constant for $Ha \rightarrow 2000$, we could potentially estimate the pressure loss in the actual WCLL manifold without recurring to direct numerical analysis.

The equivalent channel representing the external annular channel is a square channel defined such to have equal aspect ratio ($\alpha = 1$), characteristic length, and wall conductance ratio with respect to the numerical model. Regarding the internal channel, the same geometry and conductance ratio with respect the numerical model are used. Since the mass flow rate is imposed, the mean velocity for the equivalent model of the external annular channel is going to be smaller than for the numerical model. This modeling oddity is, of course, not present for the internal channel.

Errore. L'origine riferimento non è stata trovata. shows the corrective factor trend with the magnetic field intensity for the coupled internal channel (orange line), the coupled external channel (blue line) and the uncoupled external channel (green line, from Ref.[9]). The coupled trends are relative to an equally distributed mass flow rate in the channels ($\Gamma_e = \Gamma_i = 0.5\Gamma_{tot}$), whereas the uncoupled line, reported from [9], corresponding to $\Gamma_e = \Gamma_{tot}$. The brackets refer to the $Ha = 2000$ and show the dispersion of the correction factor as a function of the flow distribution between the two manifold channels. For all the cases, $\varepsilon_{e,i}$ is observed to converge to an almost constant value for $Ha > 1000$ and this is particularly true for the coupled configuration.

As shown in the figure, the pressure gradient in the internal channel is more than double by coupling phenomena, neglected in Ref. [16], (2.41 for $\Gamma_i = 0.5\Gamma_{tot}$). Dispersion with flow distribution is quite limited ranging from 2.35 (cfr. $\Gamma_i = \Gamma_{tot}$) to 2.52 ($\Gamma_i = 0.25\Gamma_{tot}$) and reflects the less sensitivity of the internal channel to coupling that was highlighted in Section 3.

Similarly, the pressure gradient for the external annular geometry increases due to coupling compared with the data reported in Ref. [9], where $\varepsilon \approx 1.12$. A much larger dispersion with flow distribution is observed for ε compared with the internal channel, which ranges from 1.42 (cfr. $\Gamma_e = \Gamma_{tot}$) to 1.92 (cfr. $\Gamma_e = 0.25\Gamma_{tot}$). Maximum increase in loss is again observed for the lower value of flow rate in the interested channel, even if the effect is smaller compared with the inner duct.

Due to the constant trend of $\varepsilon_{e,i}$, it is conceivable to estimate the pressure gradient, and consequently the pressure drop, for both the internal and external channel of a co-axial channel geometry with $\alpha = 1$ and $\beta = 0.344$ for $Ha > 1000$ by calculating the pressure loss in the equivalent square channel and multiplying it by the appropriate correction factor ($\varepsilon_{e,i}$) without the need to perform a numerical simulation. However, it should be noted that the corrective factors deduced from these calculations are strictly valid only for the chosen aspect and blockage ratio. Application to similar yet different geometries, as performed in Ref. [17], should be considered carefully and regarded as no more than a very rough estimate.
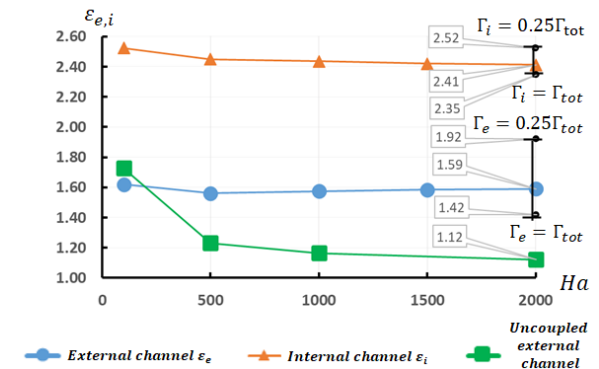

Fig. 9 Correction factor $\varepsilon_{e,i}$ trend relative to repartition of the flow rate $\Gamma_e = \Gamma_i = 0.5\Gamma_{tot}$ for the coupled cases and relative to

$\Gamma_e = \Gamma_{tot}$ for the external uncoupled case. Brackets show the range of $\varepsilon_{e,i}$ relative to $Ha = 2000$ when the distribution of flow rate varies.

5. Conclusions and follow up

The MHD forced convection flow in co-axial rectangular coupled channels is investigated with ANSYS CFX 18.2 code to a Hartmann number up to 2000. The coupling phenomena leads to several changes in the flow features for this geometry that depends on both the Hartmann number and the repartition of mass flow rate between the external and the internal channel.

The internal channel is less affected by the coupling, maintaining the classic features of MHD flow in an electroconductive rectangular channel, except in the case where the liquid metal is initially stagnant, where a reverse-flow is generated with respect to the external channel. Instead, the external channel is dominated by the coupling already for small values of internal flow rate, showing high-velocity reverse jets in correspondence of the shared side walls and complex reconfiguration of the core region.

The pressure gradient for both the external and internal channels has been correlated with the pressure gradient of an equivalent square channel, thus developing a correction factor ($\varepsilon_{e,i}$) that, being constant for $Ha > 1000$, should allow to estimate the pressure drop in the manifold at higher Hartmann numbers without performing a numerical simulation.

However, it should be noted that it is unclear how much $\varepsilon_{e,i}$ is affected by the model geometrical parameters, namely a/b, β, and c_w. Follow up activities will be focused on extending the co-axial channel characterization to include a wider range for these parameters, including non-uniform values of the conductance ratio, that are expected to influence the coupling phenomena.

Acknowledgments

References

[1] A. Del Nevo, P. Arena, G. Caruso, P. Chiovaro, P.A. Di Maio, M. Eboli, F. Edemetti, N. Forgione, R. Forte, A. Froio, F. Giannetti, G. Di Gironimo, K. Jiang, S. Liu, F. Moro, R. Mozzillo, L. Savoldi, A. Tarallo, M. Tarantino, A. Tassone, M. Utili, R. Villari, R. Zanino, E. Martelli, Recent progress in developing a feasible and integrated conceptual design of the WCLL BB in EUROfusion project, Fusion Eng. Des. 146 (2019) 1805–1809. https://doi.org/10.1016/j.fusengdes.2019.03.040.

[2] H. Madarame, K. Taghavi, M.S. Tillack, Influence of Leakage Currents on Mhd Pressure Drop., Fusion Technol. 8 (1985) 264–269.

[3] K.A. McCarthy, M.A. Abdou, Analysis of liquid metal MHD flow in multiple adjacent ducts using an iterative method to solve the core flow equations, Fusion Eng. Des. 13 (1991) 363–380. https://doi.org/10.1016/0920-3796(91)90092-5.

[4] S. Molokov, Fully developed liquid-metal flow in multiple rectangular ducts in a strong uniform magnetic field, Eur. J. Mech. B. Fluids. 12 (1993) 769–787.

[5] M.J. Bluck, M.J. Wolfendale, An analytical solution to electromagnetically coupled duct flow in MHD, J. Fluid Mech. 771 (2015) 595–623. https://doi.org/10.1017/jfm.2015.202.

[6] C. Mistrangelo, L. Bühler, Electro-magnetic flow coupling for liquid metal blanket applications, Fusion Eng. Des. 109–111 (2016) 1452–1457. https://doi.org/10.1016/j.fusengdes.2015.11.052.

[7] P.K. Swain, A. Shishko, P. Mukherjee, V. Tiwari, S. Ghorui, R. Bhattacharyay, A. Patel, P. Satyamurthy, S. Ivanov, E. Platacis, A. Ziks, Numerical and experimental MHD studies of Lead-Lithium liquid metal flows in multichannel test-section at high magnetic fields., Fusion Eng. Des. 132 (2018) 73–85.

[8] H. Chen, T. Zhou, H. Zhang, Z. Meng, Numerical investigation of liquid metal magnetohydrodynamic flow in multilayer flow channel inserts, Fusion Eng. Des. 88 (2013) 2939–2944. https://doi.org/10.1016/j.fusengdes.2013.06.006.

[9] S. Siriano, A. Tassone, G. Caruso, A. Del Nevo, MHD forced convection flow in dielectric and electro-conductive rectangular annuli, Fusion Eng. Des. 159 (2020) 111773. https://doi.org/10.1016/j.fusengdes.2020.111773.

[10] A. Tassone, G. Caruso, A. Del Nevo, Influence of PbLi hydraulic path and integration layout on MHD pressure losses, Fusion Eng. Des. 155 (2020) 111517. https://doi.org/10.1016/j.fusengdes.2020.111517.

[11] D. Martelli, A. Venturini, M. Utili, Literature review of lead-lithium thermophysical properties, Fusion Eng. Des. 138 (2019) 183–195. https://doi.org/10.1016/j.fusengdes.2018.11.028.

[12] U. Müller, L. Bühler, Magnetofluiddynamics in Channels and Containers, I, Springer-Verlag Berlin Heidelberg, 2001. https://doi.org/10.1007/978-3-662-04405-6.

[13] ANSYS Inc., ANSYS CFX Solver Theory Guide 18.2, ANSYS, 2017.

[14] ANSYS Inc., ANSYS CFX Solver Modeling Guide 18.2, ANSYS, 2017.

[15] J. Priede, T. Arlt, L. Bühler, Linear stability of magnetohydrodynamic flow in a square duct with thin conducting walls, J. Fluid Mech. 788 (2016) 129–146. https://doi.org/10.1017/jfm.2015.709.

[16] J. Reimann, G. Benamati, R. Moreau, Report of working group MHD for the blanket concept selection exercise (BSE), Karlsruhe, 1995. https://publikationen.bibliothek.kit.edu/270038027.

[17] A. Tassone, S. Siriano, G. Caruso, M. Utili, A. Del Nevo, MHD pressure drop estimate for the WCLL in-magnet PbLi loop, Fusion Eng. Des. 160 (2020) 111830. https://doi.org/10.1016/j.fusengdes.2020.111830.